Orientation Controlled Large Area Epitaxial PbI_2 Thin Films with Tunable Optical Properties

Debjit Ghoshal[1], Hanzhi Shang[2], Xin Sun[2], Xixing Wen[2], Dongxue Chen[1], Tianmeng Wang[1], Zonghuan Lu[2], Tushar Gupta[3], Harry Efstathiadis[4], Damien West[2], Nikhil Koratkar[3, 5], Toh-Ming Lu[2], Shengbai Zhang[2] and Su-Fei Shi[1, 6]

[1]Department of Chemical and Biological Engineering, Rensselaer Polytechnic Institute, Troy, NY, 12180, United States.
[2]Department of Physics, Rensselaer Polytechnic Institute, Troy, NY, 12180, United States.
[3]Department of Mechanical, Aerospace and Nuclear Engineering, Rensselaer Polytechnic Institute, Troy, NY, 12180, United States.
[4]Colleges of Nanoscale Science and Engineering, State University of New York Polytechnic Institute, Albany, NY, 12203 USA.
[5]Department of Material Science and Engineering, Rensselaer Polytechnic Institute, Troy, NY, 12180, United States.
[6]Department of Electrical, Computer, and Systems Engineering, Rensselaer Polytechnic Institute, Troy, NY, 12180, United States.

*shis2@rpi.edu

Lead Iodide (PbI_2) as a layered material has emerged as an excellent candidate for optoelectronics in the visible and ultraviolet (UV) regime. Micrometer sized flakes synthesized by mechanical exfoliation from bulk crystals or by physical vapor deposition (PVD) have shown plethora of applications from low threshold lasing at room temperature to high performance photodetectors with large responsivity and faster response. However, large area, centimeter sized growth of epitaxial thin film of PbI_2 with well controlled orientation has been challenging. Additionally, the nature of grain boundaries in epitaxial thin films of PbI_2 remains elusive. Here, we use mica as a model substrate to unravel the growth mechanism of large area epitaxial PbI_2 thin film. The partial growth leading to uncoalesced domains reveal the existence of inversion domain boundaries in epitaxial PbI_2 thin films on mica. Combining the experimental results with first-principle calculations, we also develop an understanding of the thermodynamic and kinetic factors that governs the growth mechanism, which paves the way for the synthesis of high quality large area PbI_2 on other substrates as well as heterostructures of PbI_2 on single crystalline graphene. The ability to reproducibly synthesize high quality large area thin films with precise control over orientation and tunable optical properties could open up unique and hitherto unavailable opportunities for the use of PbI_2 and its heterostructures in optoelectronics, twistronics, substrate engineering and strain engineering.

Lead Iodide (PbI_2), a layered semiconductor, has recently attracted much attention due to its unique electronic and optical properties [1–4]. In stark contrast to other layered semiconductors like MoS_2 and WS_2, which are indirect bandgap beyond the monolayer limit, multilayers of PbI_2 possess a direct bandgap, making it an ideal candidate for applications in thin film optoelectronics and energy harvesting devices [5–8]. PbI_2 has a direct bandgap of 2.4 eV and has been extensively used for applications in X-Ray and Gamma ray detection [9–11]. More recently, due to its exceptional optoelectronic properties, it has found applications in light emitting diodes (LEDs) and photodetectors in the visible range [12–14]. Ultrathin flakes of PbI_2, have also demonstrated low-threshold lasing at room temperature [15–17]. It has found applications in strain engineering [18]. It is worth noting that PbI_2 has also been effectively used as a precursor for perovskite and 2D perovskite growth [19,20]. While micrometer sized flakes have been synthesized by top down approaches (mechanical exfoliation and liquid phase exfoliation), these methods suffer from the lack of scalability for practical applications[21–23]. Although large area continuous thin films have been grown by solution and vapor based deposition techniques, their domain sizes have been small, leading to detrimental effects on the device performance due to scattering at the grain boundaries. Precise control over orientation of growth has been challenging but is critical for growing either thin films with no grain boundaries (single crystals) or with minimized grain boundaries for better device performance.

Vapor deposition has emerged as a scalable technique for large area growth of 2D materials [24,25]. Vapor based epitaxial growth has been conventionally used to grow thin films of materials with controlled orientation and minimal grain boundaries [26–29]. However, finding a substrate for conventional epitaxial growth has been demanding due to the strict lattice matching requirements for the epitaxial process [30,31]. Additionally, the strong chemical bonding at the interface between the epilayer (film) and the substrate leads to defects at the interface and propagates through the thickness, leading to poorer quality films [32]. Van der Waals (vdW) epitaxy, in which the epitaxial process is driven by weak vdW forces, has been able to circumvent both problems. Potential fields from vdW substrates are sufficiently weak to ensure relaxed lattice matching requirements but are strong enough to dictate control over crystal orientation of the epilayer, leading to epitaxial thin films of higher quality [30,31]. Mica, a “pseudo vdW” substrate, is readily available, durable, stable at high temperatures, and flexible, making it ideal for flexible optoelectronics. As such, we use mica as a model substrate for unraveling the mechanism for epitaxial growth of PbI_2 thin film.

This understanding of the growth mechanism also paves way for the fabrication of high quality heterostructures of epitaxial PbI_2 on graphene, opening up avenues for transfer of large area epitaxial PbI_2 thin films on arbitrary substrates for optoelectronics.

In this paper, we demonstrate a facile strategy for the growth of high-quality large-area epitaxial thin films of PbI_2 on mica by physical vapor deposition (PVD) method. Using electron back scatter diffraction (EBSD), we study the nature of grain boundaries in these epitaxial thin films. Although azimuthal X-ray and scanning transmission electron microscopy (STEM) diffraction show six-fold symmetry, we reveal the existence of inversion domains in these films which are formed due to the coalescence of 0^o and 180^o domains. The influence of growth rate of the films on the crystallographic and optical properties of the film are also investigated. Using azimuthal X-ray scans, we demonstrate higher quality epitaxial films with narrower spread in the in-plane direction for slower growth rate of the films. We also investigate the influence of the growth rate on the photoluminescence (PL) from PbI_2 thin film. While slow growth leads to narrow PL peak centered at 496 nm, samples grown at higher ramping rates show a broader red shifted PL peak at 598 nm. Using Photoluminescence excitation (PLE) spectrocopy and time resolved photoluminescence (TRPL) spectrocopy, we demonstrate that the emission at 496 nm is of excitonic origin while the redshifted emission at 598 nm, which dominates the spectrum in samples with a faster growth rate, is possibly from defects. The greater defect density in epitaxial films grown at faster ramping rates, clearly underlines the importance of kinetics of growth in epitaxial films in determining the crystallographic and optical properties of the PbI_2 film.

Finally, the quality of the epitaxial thin films grown using different single crystalline substrates (mica, graphene and sapphire) are compared. While graphene has the weakest interactions with PbI_2 (vdW), sapphire interacts most strongly (chemical bonds). Mica being a "pseudo" vdW is somewhere inbetween. Interestingly, while all three substrates lead to highly ordered thin films, PL measurements reveal the presence of defects in the film grown with the strongest interaction (sapphire), likely due to strain induced defects introduced during the growth process. Our work unravels the importance of thermodynamics (choice of substrate) and kinetics (growth rate) in the growth of epitaxial thin films of semiconducting layered materials. While kinetics plays a critical role in determining the quality of epitaxial films for substrates with stronger interaction (mica and sapphire), the use of a graphene as a buffer layer for vdW epitaxy enables

growth of high quality defect free epitaxial films on an amorphous substrate even at extremely fast growth rates. Additionally, the use of vdW substrate would enable easy peel off and transfer of the high quality epitaxial film onto an arbitrary substrate, paving way for fabrication of various functional devices. Therefore, our work provides insight into the mechanism for growth of epitaxial thin films of PbI_2, which guides the synthesis of high-quality large area epitaxial thin films of layered materials with controllable orientation and tunable optical properties.

RESULTS AND DISCUSSION

The PbI_2 thin film is grown by our home-built low-pressure physical vapor deposition (LPPVD) setup. The process is described briefly as follows. Fleshly cleaved mica sized at 1 cm x 1 cm is used as a growth substrate. The growth substrate is placed downstream inside a quartz tube. Lead Iodide (PbI_2) pellets are heated in a ~1 inch tube furnace at a temperature of ~370^{o}C. The furnace is purged with ultrahigh purity (UHP) Argon gas for about 20 minutes prior to the heating stage with a flow rate of 30 sccm. UHP Argon flow rate is maintained at 30 sccm during the heating stage where Argon serves as a transport gas. The temperature ramping rate is varied between 3^{o}C/min (slow growth) to 37^{o}C/min (fast growth). The furnace is maintained at a temperature of 370^{o}C for 10 minutes once it reaches that temperature. The pressure is maintained at around 650 mtorr during the growth process. A schematic of the furnace used for the growth process as well as the temperature profile inside the furnace are illustrated in the Supplementary Information (Fig. S1). Fig. 1a shows the photograph of the film (left) as well as the bare substrate mica (right). While the sample with bare mica appears transparent, a smooth uniform yellow deposition is observed on the sample coated with PbI_2. Fig. 1b shows an optical microscope image of the film. Highly oriented PbI_2 domains can be seen from the optical images. Scanning electron microscope (SEM) image (Fig. 1c) also shows a continuous smooth film with ordered PbI_2 domains with domain sizes typically of hundreds of microns. XRD measurements of the films were performed to obtain information on the crystal structure of the film. The θ-2θ XRD measurements (Fig. 1d) confirmed the {001} peaks in the out-of-plane direction. Rocking curves were collected with θ parked at 24.8^o showed a FWHM of 0.15^o confirming narrow spread in the out-of-plane direction (Fig. 1e). In order to get information about the quality of the crystal in the in-plane direction, X-ray pole figure measurements were done and shown in Fig.1f. The X-Ray pole figure measurements at 2θ of 24.8^o showed six discrete spots azimuthally separated by 60^o at

a tilt angle (χ) of 62°. The six spots confirmed the in-plane order in the deposited film. The theoretical pole figure is shown in Fig. S2 (see SI) and has 6 spots suggesting the growth of single crystalline film. FWHM of peaks from azimuthal scans at a tilt angle of 62° (Fig. 1g) confirmed narrow dispersion in the in-plane direction and showed six fold symmetry similar to the findings in the pole figure, suggesting single crystal nature of the film. However, various aligned boundaries (Fig. 1b and Fig. 1c) in optical and SEM images of the film contradict the idea of a perfect single crystalline film.

Further characterization was done to get more information on the nature of the films. High resolution STEM images confirmed the crystal structure of PbI_2 as shown in Fig. 2a. A higher magnification image from the black square part is shown in Fig. 2b, clearly showing the arrangement of the individual atoms. The fast fourier transform (FFT) from the STEM images is shown in Fig. 2c, which shows six spots again pointing to local single crystalline nature of the film. Raman measurements (Fig. 2d) showed peaks at 73 cm^{-1}, 95 cm^{-1} and 111 cm^{-1}, consistent with previous literature confirming the synthesis of PbI_2 thin films. Photoluminescence (PL) measurements at room temperature confirm an optical bandgap of 2.43 eV, consistent with previous literature (Fig. 2e).

While XRD pole figures and FFT images from STEM pointed to six fold symmetry consistent with single crystal PbI_2, the presence of oriented domains from the optical and SEM images paints a different picture. In order to probe the nature of the oriented boundaries in these films, samples were grown for shorter durations and their orientations were probed using EBSD measurements. The partial growth (as a consequence of shorter growth periods) resulted in the formation of uncoalesced PbI_2 triangles and truncated triangles of different thicknesses. In rare cases, hexagons were also seen. As can be seen from the SEM image shown in Fig. 3a as well as optical and atomic force microscope (AFM) image Fig. S3 (see SI), two major configurations can be seen before their coalescence to form a film, triangles pointing up and pointing down, as also shown in the SEM image in Fig. 3a. Fig. 3b shows a phase mapping with the yellow parts showing the substrate region while the red parts corresponding to the PbI_2 flakes on the substrate. The inverse pole figure (IPF) mappings from the same area are shown in Fig. 3c-e. The homogeneous colors on the IPF mappings confirm perfect single crystallinity of each triangle. Interestingly, while the IPF Z orientation is the same (001) for both the triangles, which is consistent with the

XRD data, in the in-plane direction the triangles are rotated by 180°, thus resulting in mirror twin domains. Thus, while XRD and STEM demonstrate limitations in predicting the nature of oriented boundaries present in our samples, EBSD unambiguously identifies the presence of mirror twin domains in our uncoalesced films. The oriented boundaries in the continuous film possibly originate from the coalescence of these mirror twin domains originating from the triangles pointing upward and downward. The EBSD pole figures from the two orientations are shown in Fig. 3f. While EBSD measurements on the uncoalesced domains confirm the existence of mirror twin domains, the nature of each domain boundary in the coalesced film still needs to be confirmed. STEM measurements at these grain boundaries can confirm the exact nature of the boundaries and needs to be investigated. The existence of some translational grain boundaries in such incommensurate epitaxial films cannot be ruled out. As expected, EBSD mapping inside a single domain in a continuous film resulted in a homogeneous color and is shown in Fig. 3g-k. The IPF Z, IPF X and IPF Y mappings show single crystal nature inside a single domain. Larger area maps of single crystal domains are shown in SI (Fig. S4), which have some spots with no EBSD signal due to some roughness associated with the surface.

Several reports have demonstrated direct influence of the growth rate of the films on the quality of the films in epitaxial processes. In order to investigate the influence of kinetics of growth on the epitaxial process, films were grown at much faster rates (ramping rates of 37°C/min). The crystal quality of these films grown at much faster rates was investigated with XRD measurements. The peak in the out-of-plane orientation was still found to be {001}, similar to the samples that were grown at slower ramping rates (3°C/min). The FWHM of the rocking curve was also found to be of similar value (0.15°) as shown in Fig. 4a, demonstrating similar dispersion in the out of plane direction. Interestingly, pole figure measurements showed 12 spots separated azimuthally by 30° at the tilt angle of 62° demonstrating the presence of additional domains in the in-plane direction (Fig. 4b).

Geometrical superlattice area mismatching (GSAM) simulation was performed to calculate possible favorable orientational alignments between PbI_2 and mica [33–36]. During the simulation, the superlattice vectors of PbI_2 overlayer (mica substrate) were defined as u_1 and v_1 (u_2 and v_2), which were separated by a rotational angle, α_1 (α_2). All the superlattices possibly formed between PbI_2 and mica are calculated by adjusting the rotation angle (ϕ_R) from 0° to 360°, where ϕ_R is

defined as the angle between PbI_2 $[2\bar{1}\bar{1}0]$ and mica [100] directions. Two criteria are used in the calculation to determine the relative likelihood of observing a superlattice at a given ϕ_R: (a) the superlattice area of PbI_2, A_1 (the superlattice area of mica, A_2) should be small to increase the density of near coincident lattice sites; (b) the mismatch between the two superlattices A_1 and A_2, denoted as ΔA, should be small to minimize the heteroepitaxial system's interfacial strain energy [1,2]. The ΔA is defined as:

$$\Delta A = A\,(\Delta u/u + \Delta v/v + \Delta\alpha/\tan\alpha), \quad (1)$$

where $\Delta u=|u_1-u_2|$, $\Delta v=|v_1-v_2|$ and $\Delta\alpha=|\alpha_1-\alpha_2|$ are the differences of superlattice parameters between PbI_2 and mica, and $A\approx A_1$ (or A_2), $u\approx u_1$ (or u_2), $v\approx v_1$ (or v_2), $\alpha\approx\alpha_1$ (or α_2). The following limits are set to exclude those improbable rotation angles for forming superlattices: $\Delta u/u \leq 10\%$, $\Delta v/v \leq 10\%$, and $\Delta\alpha/\alpha \leq 5\%$, and A_1 (or A_2) ≤ 200 Å^2. Based on the criteria mentioned above, the rotation angle ϕ_R associated with the smallest values of A_1 (A_2) and ΔA represents the desirable condition for a superlattice to form at the interface.

Fig. 4c shows the calculated ΔA, smaller than 25 Å^2 using the lattice constants of $\vec{a}_{PbI_2}$= 4.69 Å and $\vec{a}_{mica}$= 5.19 Å. The radius of the circles in Fig. 1(a) is scaled inversely proportional to A. In the plot, the smallest ΔA of 4.49 and 6.08 Å^2 occur at ϕ_R of 0º and 30º, respectively. It indicates that the heteroepitaxial PbI_2 on mica has two favorable domains. This calculation is consistent with what is observed experimentally in the measured pole figure. Fig. 4 d-e show the 2D lattice overlay of the two most favorable alignment of PbI_2(0001) on mica. For the ϕ_R = 0º, as shown in Fig. 1(b), the superlattice parallelograms (highlighted in blue) of PbI_2(0001) and mica are defined as A_1 = 19.05 Å^2, u_1 = 4.69 Å, v_1 = 8.12 Å, α_1= 30º and A_2 = 23.33 Å^2, u_2 = 5.29 Å, v_2 = 8.99 Å, α_2= 30º, respectively. Fig. 1(c) shows the superlattice parallelograms (highlighted in light blue) of PbI_2(0001) and mica at ϕ_R = 30º, defined as A_1 = 76.2 Å^2, u_1 = 16.25 Å, v_1 = 9.38 Å, α_1= 30º and A_2 = 69.98 Å^2, u_2 = 15.57 Å, v_2 = 8.99 Å, α_2= 30º, respectively. Interestingly, the findings from the GSAM calculations compliment the experimental findings and demonstrate that the 0º and 60º (or 180º) are the most favorable domains. Additionally, it also shows that the 30^0 domains are also favorable, which is also observed experimentally in the films grown at higher ramping rates. However, GSAM results are only suggestive and kinetic effects are not captured in GSAM

calculations and hence, these results do not clarify the predominance of the 30° domains at higher ramping rates.

To unravel the origin of the 30° domains at higher ramping rates, we have performed first-principles total-energy calculations to analyze our experimental results. The structure of mica is shown in Fig. S5. After cleavage, the ionic bonds between the K layer and layers below made of Si, Al, and O will be broken, as shown in Fig. S5b. Importantly, some of the surface K atoms will be removed during the cleavage in order to minimize the surface energy, as our calculation reveals that the stable insulating surface should have only half K coverage. Beneath the K, there are also two different types of SiAl rings, namely, the Si_4Al_2 and Si_5Al_1 rings, shown in Fig S6. Our calculation shows that the K atoms prefer to sit on the Si_4Al_2 rings, with an energy lowering of 0.12 eV/K. Next, we place PbI_2 in units of hexagonal rings on the mica surface. To our surprise, however, such a self-passivated mica surface is still reactive, leading to significant deformation and even dissociation of the PbI_2 rings to fill up the K-missing rows (or troughs) of the surfaces. Experimentally, it is known that the troughs on the surface are often covered by oxides (of still unknown structures) [37]. For simplicity, here we cover the surface with PbI_2 molecules before examining the growth of the PbI_2 monolayer film. This leads to the structure shown in Fig. S7, where the Pb atoms occupy the vacant sites by the missing K atoms. Note here that this surface reconstruction possesses long-range order that lowers the symmetry and leads to slight differences in the 0º and 60º orientation energies. We find that PbI_2 molecules preferentially fill these vacant sites, with a binding energy of 2.43 eV/PbI_2 as opposed to forming intact rings on the reactive surface with a total energy (formation and binding) of only 1.02 eV/PbI_2. This suggests that the vacant sites are completely filled before nucleation of bulk PbI_2 on the self-passivated mica surface.

We consider PbI_2 rings (see Fig. 5(d)) as the basic nucleation centers for the film growth. To investigate the energetics of the various orientations of these nucleation centers, we calculate the ring at different positions on the surface: T1, T2, T3, T4, H1, and H2, shown in Fig. 5a with different orientations. Here, T stands for a "top" position, while H stands for a "hexagonal center" position of the underneath substrate. Fig. 5b depicts the lowest energy positions among the various adsorption sites as a function of the orientation of the ring with respect to that of the substrate. There are three orientations to consider here for the initial growth: 0º, 30º, and 60º. The 0º is found

to be the global energy minimum with 0.462 eV/PbI_2 binding energy, the 60º orientation follows with a rather similar binding energy of 0.443 eV/PbI_2. In contrast, the 30º has a notably smaller binding energy of 0.344 eV/PbI_2 to the surface. The large binding for the 0º and 60º orientations is found to be a result of a strong binding of the edge of the PbI_2 ring to the metal atoms on the substrate, see for example Fig. 5c. Under slow growth conditions, with long enough time for the deposited PbI_2 to find the lowest energy geometry on the substrate, the 0º and 60º structures will dominate the growth. When the deposition rate is high, however, nucleation centers with orientations of 30º can grow quickly and become kinetically trapped, unable to rotate to the more stable 0º or 60º orientations. As such, at the higher deposition rates, both 0º and 30º orientations are seen in experiment, with the more energetic 30º structure growing somewhat faster and existing in larger quantities.

PL measurements were performed on these epitaxial films and the influence of growth rates on the optical properties of the films was evaluated. PL measurements on the sample grown at slower ramping rates (3ºC/min) show a sharp peak centered around 494 nm (Fig. 6a). The florescence image from the sample is shown in the inset of Fig. 6 a. Interestingly, samples grown at faster ramping rates show very different emission properties. As can be seen in Fig. 6b, samples grown at much faster ramping rates (37ºC/min) show a broader PL peak centered at 598 nm. The florescence image (inset of Fig. 6b) shows a red emission in stark contrast to the green emission from the samples grown at slower ramping rates of 3ºC/min. The lifetime dynamics of the two peaks are also found to be very different. While the PL peak at 494 nm (predominant in the 3ºC/min sample) is found to have a shorter lifetime of 0.350 ±.009 ns, the broad peak at 598 nm (dominant in 37ºC/min sample) is found to have an order of magnitude longer lifetime of 3.9±0.03 ns (Fig. 6c). The longer lifetime as well as the broadness of the peak could be attributed to defect states in the PbI_2 films. In order to confirm the origin of the two peaks, PLE measurements were performed on the sample with higher ramping rate where the excitation was varied from the 450 nm to 590 nm and the emission from the sample was measured as a function of the excitation photon energy (Fig. 6d). Interestingly, it was found that the emission at 598 nm from the sample was enhanced when the excitation photon wavelength was 494 nm i.e. in resonance with the sharp peak observed in the first sample (grown at slower ramping rate), suggesting excitonic absorption centered at 494 nm. However, no PL emission was observed in the PbI_2 films when the excitation wavelength was

longer than 496 nm, possibly due to the negligible direct absorption from the defect state because of weak oscillator strengths. The ingap defect state is possibly populated due to the communication with the higher energy states and can only be observed when the excitation energy is greater than the bandgap or in resonance with the excitonic state in the film. The integrated PL intensity for the PLE measurement is shown in Fig. 6e. The pronounced peak at 494 nm in the integrated PL measurements further confirms the excitonic origin of the peak.

Quality of the epitaxial films is significantly influenced by the substrate they are grown on and the nature of interactions between the film and the substrate. Our experimental results and theoretical understanding suggest that an ideal substrate would have appropriate interaction: enough to ensure epitaxy growth but not too strong to result in strain induced defects. To test this hypothesis, we further performed the growth of PbI_2 on two other substrates other than mica. Single crystal graphene was chosen as a pure vdW substrate (appropriate interaction) while sapphire was chosen as a model substrate for conventional epitaxy where chemical bonds exist between the substrate and the film (thus strong interaction). The crystal quality of the films grown on single crystal graphene transferred to amorphous SiO_2 substrate is shown in Fig. 7. The results of these films grown on bare SiO_2 (without the graphene buffering layer) are also shown in Fig. 7a and Fig. 7b. The θ-2θ measurements (Fig. 7a) confirmed the {001} out of plane direction. Interestingly, θ-2θ scans for SiO_2 without the graphene buffering layer also showed similar peak positions but the intensities of the peaks are weaker, signifying poorer crystallinity. Rocking curves for samples grown on bare SiO_2 show a very broad peak with FWHM of 3.1°, typical of amorphous films with fiber texture. The presence of graphene buffer layer results in remarkable improvement in crystallinity of the film grown the same amorphous SiO_2 substrate with FWHM for the rocking curves 0.13° (Fig. 7b). Phi scans (Fig. 7c) at a tilt angle of 62° confirmed the high-quality of the crystal in the in-plane direction with six fold symmetry. The phi scans also confirm the parallel epitaxy with respect to graphene. GSAM predictions, shown in Fig. 7d and Fig. 7e confirmed 0° and 60° as the most favorable theoretical predictions in sync with the experimental findings. All these results confirm large area high-quality epitaxial films on an amorphous substrate (SiO_2) buffered with single crystal graphene, opening up possibilities direct growth of heterostructures of these materials and fabrication of highly efficient optoelectronic devices.

Epitaxial films of PbI_2 were also grown on sapphire and the rocking curve and phi scan is shown in Fig. S8. The PL measurements on the films grown on all the three substrates at the same growth conditions are shown in Fig. S9. Clearly, substrates with stronger interactions (both mica and sapphire) show a broader defect peak while the samples with weaker interaction (graphene) show a very strong excitonic peak. These results emphasize the importance of use of buffer layer graphene as a vdW substrate for growth of epitaxial films. The use of a true vdW substrate (graphene) enables high-quality epitaxial thin films of PbI_2 even at extremely fast growth rates. They also allow the facile transfer of these films onto arbitrary substrates due to weak vdW interactions.

CONCLUSIONS

In conclusion, we demonstrate the growth of high-quality large area epitaxial PbI_2 with controlled orientations on mica. We study the nature of grain boundaries in these epitaxial thin films by looking into the domain orientations in uncoalesced films. We show the importance of kinetics (growth rate) on the epitaxial growth process and how faster kinetics can lead to poorer film quality. We also unambiguously identify the influence of substrate on the thermodynamics of the growth process. While weaker interactions (pure vdW) with the substrate lead to high quality films (like in graphene), stronger interactions (pseudo vdW in mica and chemical interactions in sapphire) lead to poorer quality of films with defects. The epitaxial films thus show drastic differences in PL emission when grown on different substrates opening up applications of substrate engineering to tune optoelectronic properties of the material. Thus, mica serves as an excellent substrate to understand the mechanism for growth due to its consistency in quality and intermediate interaction (Pseudo vdW). The understanding of the growth mechanism on mica also inspired the fabrication of large area epitaxial PbI_2 on graphene and other substrates. The controllable large area growth of epitaxial PbI_2 on various substrates, thorough understanding of the kinetics and thermodynamics of the growth process and ability to grow films with tunable emission properties could pave way for the use of this material as a potent material for thin film optoelectronics.

METHODS

Synthesis of PbI_2 films: PbI_2 thin film is grown in a tube reactor by PVD as described in the main manuscript. A schematic of the furnace and the growth temperature profile is provided in Fig S1.

Graphene transfer and growth on graphene: Graphene grown on Copper was transferred onto 285 nm SiO_2/ Si substrate using standard wet transfer techniques. Poly(methyl methacrylate) (PMMA) A4 is spin coated onto graphene on Copper substrate at 1500 rpm for 60 seconds followed by baking at 120^0C after each step of spin coating. Copper is etched from the spin coated material using ammonium persulfate solution (3g in 50 ml of water). The graphene/PMMA stack is scooped from the solution after the copper is completely etched using a Si substrate followed by a series of rinsing in DI water. Finally the rinsed stack is scooped from DI water using 285 nm Si/SiO_2 substrate. The stack is dried in air for a few minutes. In the final step, the PMMA is dissolved in acetone and the graphene/substrate stack is rinsed in Isopropanol and dried with Nitrogen. This PbI_2 are then grown on graphene as described in the main text.

Materials characterization: SEM was performed by using a ZEISS SUPRA 55 Field emission scanning electron microscope. Tapping mode of Multimode AFM from Digital Instruments was used for obtaining the topography images. Transmission electron microscopy was carried out on a FEI Titan cubed STEM equipped with a monochromator and probe corrector. EBSD was collected with a NordlysNano detector (Oxford Instruments) integrated with a Carl Zeiss Ultra 1540 SEM/FIB system. The crystallographic orientation data were collected using the Aztec EBSD data acquisition software. XRD was measured with a Bruker D8 Discover X-ray diffractometer (Cu Kα = 1.54 Å). The beam and detector slits for XRD were both 0.6 mm.

PL and Raman measurements: Photoluminescence (PL) was measured with a home-built confocal microscope setup using lasers under different excitation conditions depending on the type of measurement. A spectrograph (Andor) and a thermoelectric cooled CCD camera (Andor) was used for the spectroscopy measurement. Raman measurements were done in the same setup. The time-resolved PL (TRPL) was measured through the time-correlated single photon counting (TCSPC) technique and an avalanche photodiode detector (APD, by Micro Photon Devices) was used. For both PL and TRPL measurements, the excitation lasers were focused to a spot size with the diameter of 2 μm.

Theoretical calculations: The calculations are carried out using density functional calculation with the PBE functional and the projected augment wave (PAW) potential method as implemented in the VASP code. The wave functions are expanded in a plane wave basis up to a cutoff energy of 300eV.

ACKNOWLEDGEMENT

S.-F.S. and N.K. acknowledge funding support from the US National Science Foundation (Award 1608171). T.W. and S.-F.S. acknowledge support from ACS PRF through Grant 59957-DNI10. S.-F. S. also acknowledges the support from NSF through Career Grant DMR-1945420. S.-F. Shi and S. Zhang acknowledge the support from an RPI KIP grant. D.G. acknowledges the Center for Materials, Devices and Integrated Systems and the Center for Future Energy Systems at Rensselaer Polytechnic Institute for access to their facilities. D. W. was supported by the NSF under Award No. EFMA-1542798. S. B. Z. was supported by the U.S. DOE Grant No. DE-SC0002623. H. S., D.W., and S. B. Z. acknowledge supercomputer time sponsored by National Energy Research Scientific Center (NERSC) under DOE Contract No. DE-AC02-05CH11231 and the Center for Computational Innovations (CCI) at RPI are also acknowledged.

REFERENCES:

[1] J. Xiao, J. Liu, K. Sun, Y. Zhao, Z. Shao, X. Liu, Y. Yuan, Y. Li, H. Xie, F. Song, Y. Gao, H. Huang, *J. Phys. Chem. Lett.* **2019**, *10*, 4203.

[2] Y. Sun, Z. Zhou, Z. Huang, J. Wu, L. Zhou, Y. Cheng, J. Liu, C. Zhu, M. Yu, P. Yu, W. Zhu, Y. Liu, J. Zhou, B. Liu, H. Xie, Y. Cao, H. Li, X. Wang, K. Liu, X. Wang, J. Wang, L. Wang, W. Huang, *Adv. Mater.* **2019**, *31*, 1806562.

[3] A. Sengupta, K. C. Mandal, J. Z. Zhang, *J. Phys. Chem. B* **2000**, *104*, 9396.

[4] C. Cong, J. Shang, L. Niu, L. Wu, Y. Chen, C. Zou, S. Feng, Z.-J. Qiu, L. Hu, P. Tian, Z. Liu, T. Yu, R. Liu, *Adv. Opt. Mater.* **2017**, *5*, 1700609.

[5] J. Zhang, Y. Huang, Z. Tan, T. Li, Y. Zhang, K. Jia, L. Lin, L. Sun, X. Chen, Z. Li, C. Tan, J. Zhang, L. Zheng, Y. Wu, B. Deng, Z. Chen, Z. Liu, H. Peng, *Adv. Mater.* **2018**, *30*, 1803194.

[6] N. Sharma, I. M. Ashraf, M. T. Khan, M. Shkir, M. S. Hamdy, A. Singh, A. Almohammedi, F. B. M. Ahmed, I. S. Yahia, S. AlFaify, *Sensors Actuators A Phys.* **2020**, *314*, 112223.

[7] R. Frisenda, J. O. Island, J. L. Lado, E. Giovanelli, P. Gant, P. Nagler, S. Bange, J. M. Lupton, C. Schüller, A. J. Molina-Mendoza, L. Aballe, M. Foerster, T. Korn, M. Angel Niño, D. P. de Lara, E. M. Pérez, J. Fernandéz-Rossier, A. Castellanos-Gomez, *Nanotechnology* **2017**, *28*, 455703.

[8] R. Wang, S. Li, P. Wang, J. Xiu, G. Wei, M. Sun, Z. Li, Y. Liu, M. Zhong, *J. Phys. Chem. C* **2019**, *123*, 9609.

[9] L. Fornaro, E. Saucedo, L. Mussio, L. Yerman, X. Ma, A. Burger, *Nucl. Instruments Methods Phys. Res. Sect. A Accel. Spectrometers, Detect. Assoc. Equip.* **2001**, *458*, 406.

[10] R. A. Street, S. E. Ready, K. Van Schuylenbergh, J. Ho, J. B. Boyce, P. Nylen, K. Shah, L. Melekhov, H. Hermon, *J. Appl. Phys.* **2002**, *91*, 3345.

[11] K. S. Shah, F. Olschner, L. P. Moy, P. Bennett, M. Misra, J. Zhang, M. R. Squillante, J. C. Lund, *Nucl. Instruments Methods Phys. Res. Sect. A Accel. Spectrometers, Detect. Assoc. Equip.* **1996**, *380*, 266.

[12] M. Zhong, L. Huang, H.-X. Deng, X. Wang, B. Li, Z. Wei, J. Li, *J. Mater. Chem. C* **2016**, *4*, 6492.

[13] Z. Qi, T. Yang, D. Li, H. Li, X. Wang, X. Zhang, F. Li, W. Zheng, P. Fan, X. Zhuang, A. Pan, *Mater. Horizons* **2019**, *6*, 1474.

[14] M. Han, J. Sun, L. Bian, Z. Wang, L. Zhang, Y. Yin, Z. Gao, F. Li, Q. Xin, L. He, N. Han, A. Song, Z. Yang, *J. Mater. Chem. C* **2018**, *6*, 5746.

[15] Y. Zhong, Q. Wei, Z. Liu, Q. Shang, L. Zhao, R. Shao, Z. Zhang, J. Chen, W.

Du, C. Shen, J. Zhang, Y. Zhang, P. Gao, G. Xing, X. Liu, Q. Zhang, *Small* **2018**, *14*, 1801938.

[16] X. Liu, S. T. Ha, Q. Zhang, M. de la Mata, C. Magen, J. Arbiol, T. C. Sum, Q. Xiong, *ACS Nano* **2015**, *9*, 687.

[17] C.-X. Sheng, Y. Zhai, E. Olejnik, C. Zhang, D. Sun, Z. V Vardeny, *Opt. Mater. Express* **2015**, *5*, 530.

[18] Y. Wang, Y.-Y. Sun, S. Zhang, T.-M. Lu, J. Shi, *Appl. Phys. Lett.* **2016**, *108*, 13105.

[19] J. C. Hill, J. A. Koza, J. A. Switzer, *ACS Appl. Mater. Interfaces* **2015**, *7*, 26012.

[20] S. M. Jain, B. Philippe, E. M. J. Johansson, B. Park, H. Rensmo, T. Edvinsson, G. Boschloo, *J. Mater. Chem. A* **2016**, *4*, 2630.

[21] S. Sinha, T. Zhu, A. France-Lanord, Y. Sheng, J. C. Grossman, K. Porfyrakis, J. H. Warner, *Nat. Commun.* **2020**, *11*, 823.

[22] Q. Fan, J. Huang, N. Dong, S. Hong, C. Yan, Y. Liu, J. Qiu, J. Wang, Z. Sun, *ACS Photonics* **2019**, *6*, 1051.

[23] P. Wangyang, H. Sun, X. Zhu, D. Yang, X. Gao, *Mater. Lett.* **2016**, *168*, 68.

[24] D. Ghoshal, T. Wang, H.-Z. Tsai, S.-W. Chang, M. Crommie, N. Koratkar, S.-F. Shi, *Adv. Opt. Mater.* **2019**, *0*, 1900039.

[25] D. Ghoshal, A. Yoshimura, T. Gupta, A. House, S. Basu, Y. Chen, T. Wang, Y. Yang, W. Shou, J. A. Hachtel, J. C. Idrobo, T.-M. Lu, S. Basuray, V. Meunier, S.-F. Shi, N. Koratkar, *Adv. Funct. Mater.* **2018**, DOI 10.1002/adfm.201801286.

[26] T.-A. Chen, C.-P. Chuu, C.-C. Tseng, C.-K. Wen, H.-S. P. Wong, S. Pan, R. Li, T.-A. Chao, W.-C. Chueh, Y. Zhang, Q. Fu, B. I. Yakobson, W.-H. Chang, L.-J. Li, *Nature* **2020**, *579*, 219.

[27] X. Li, S. Sundaram, Y. El Gmili, T. Ayari, R. Puybaret, G. Patriarche, P. L.

Voss, J. P. Salvestrini, A. Ougazzaden, *Cryst. Growth Des.* **2016**, *16*, 3409.

[28] D. Dumcenco, D. Ovchinnikov, K. Marinov, P. Lazić, M. Gibertini, N. Marzari, O. L. Sanchez, Y.-C. Kung, D. Krasnozhon, M.-W. Chen, S. Bertolazzi, P. Gillet, A. Fontcuberta i Morral, A. Radenovic, A. Kis, *ACS Nano* **2015**, *9*, 4611.

[29] D. Ghoshal, R. Jain, N. A. Koratkar, *Langmuir* **2019**, *35*, 12306.

[30] D. Mohanty, Z. Lu, X. Sun, Y. Xiang, L. Gao, J. Shi, L. Zhang, K. Kisslinger, M. A. Washington, G.-C. Wang, T.-M. Lu, I. B. Bhat, *Carbon N. Y.* **2019**, *144*, 519.

[31] D. Mohanty, Z. Lu, X. Sun, Y. Xiang, Y. Wang, D. Ghoshal, J. Shi, L. Gao, S. Shi, M. Washington, G.-C. Wang, T.-M. Lu, I. Bhat, *Phys. Rev. Mater.* **2018**, *2*, 113402.

[32] J. Jiang, X. Sun, X. Chen, B. Wang, Z. Chen, Y. Hu, Y. Guo, L. Zhang, Y. Ma, L. Gao, F. Zheng, L. Jin, M. Chen, Z. Ma, Y. Zhou, N. P. Padture, K. Beach, H. Terrones, Y. Shi, D. Gall, T.-M. Lu, E. Wertz, J. Feng, J. Shi, *Nat. Commun.* **2019**, *10*, 4145.

[33] A. S. Yapsir, C. -H. Choi, T. -M. Lu, *J. Appl. Phys.* **1990**, *67*, 796.

[34] A. Zur, T. C. McGill, *J. Appl. Phys.* **1984**, *55*, 378.

[35] X. Sun, Z. Lu, W. Xie, Y. Wang, J. Shi, S. Zhang, M. A. Washington, T.-M. Lu, *Appl. Phys. Lett.* **2017**, *110*, 153104.

[36] D. Mohanty, X. Sun, Z. Lu, M. Washington, G.-C. Wang, T.-M. Lu, I. B. Bhat, *J. Appl. Phys.* **2018**, *124*, 175301.

[37] F. Ostendorf, C. Schmitz, S. Hirth, A. Kühnle, J. J. Kolodziej, M. Reichling, *Nanotechnology* **2008**, *19*, 305705.

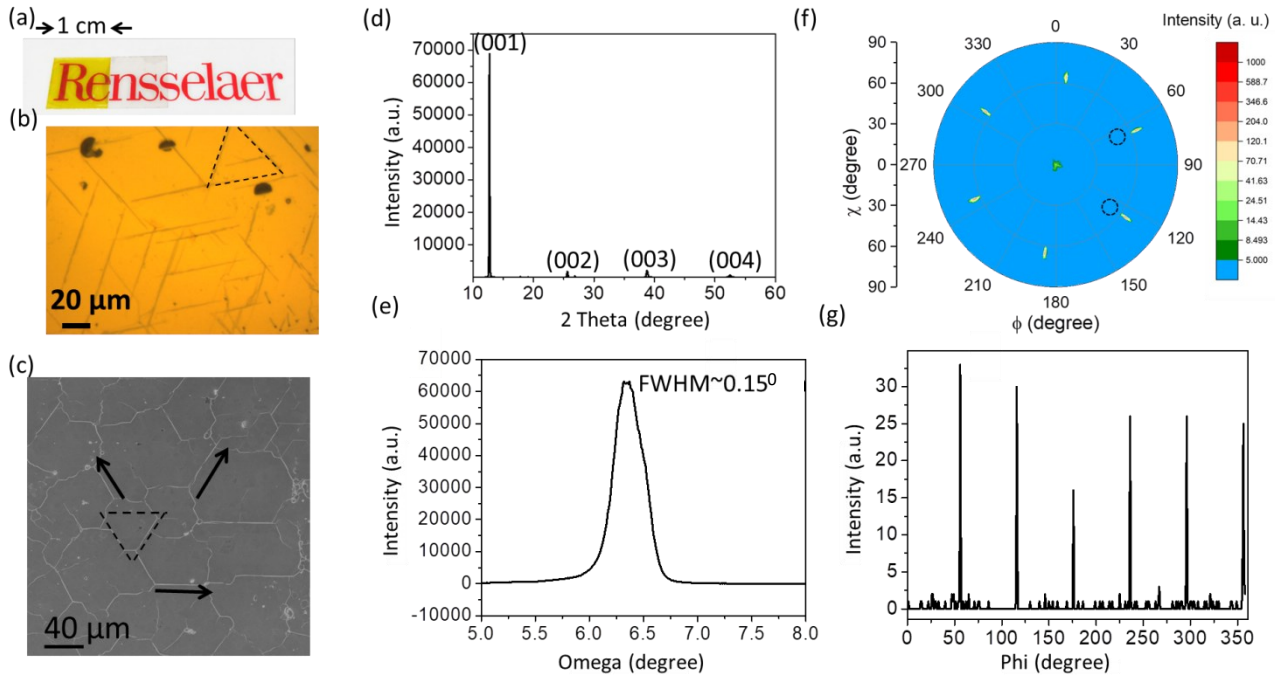

Figure 1. PbI_2 thin film characterization and crystal structure grown on mica at ramping rate of 3ºC/min. (a) Photograph of the PbI_2 film and mica substrate (b) Optical microscope image of the PbI_2 film (c) SEM image of the PbI_2 films (d) XRD 2θ scan of the PbI_2 film (d) Rocking curve showing dispersion in the out-of-plane direction (e) Pole figure of the thin film on mica (f) Phi scans showing dispersion in the in-plane direction.

.

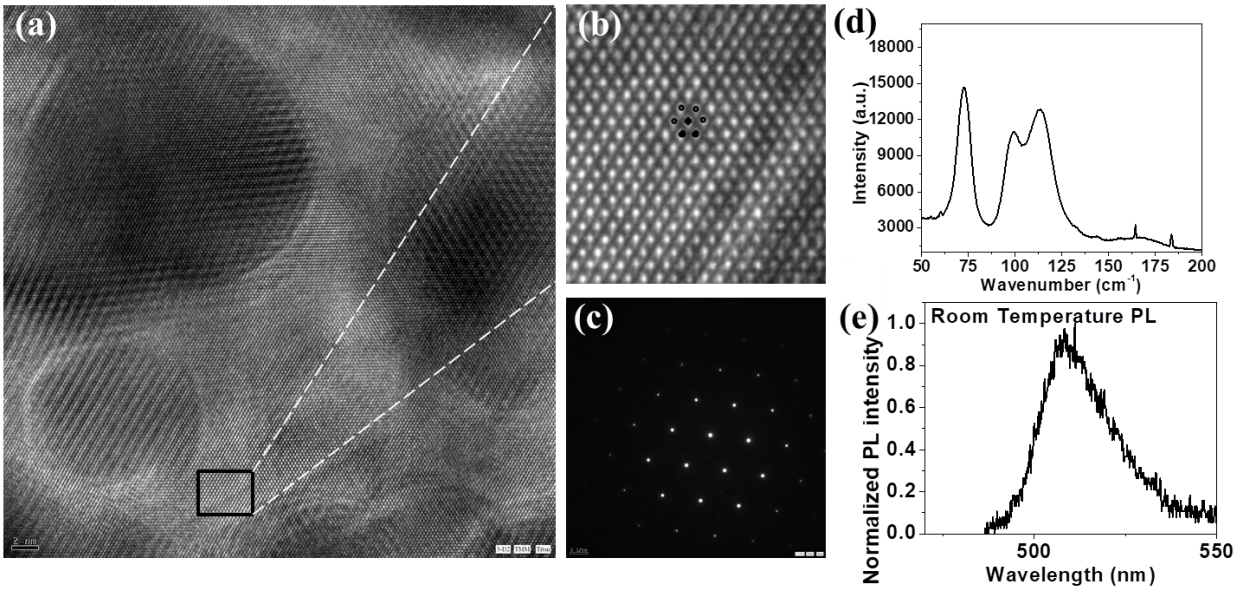

Figure 2. Characterization of PbI_2 thin films on mica. (a) TEM image of PbI_2 flake grown on mica and subsequently transferred on TEM grid (b) Higher magnification image from the area shown in black box showing individual atoms. (c) FFT pattern from the sample showing 6-fold symmetry. (d) Raman spectrum of the PbI_2 thin film. (e) PL measurement at room temperature for the PbI_2 sample.

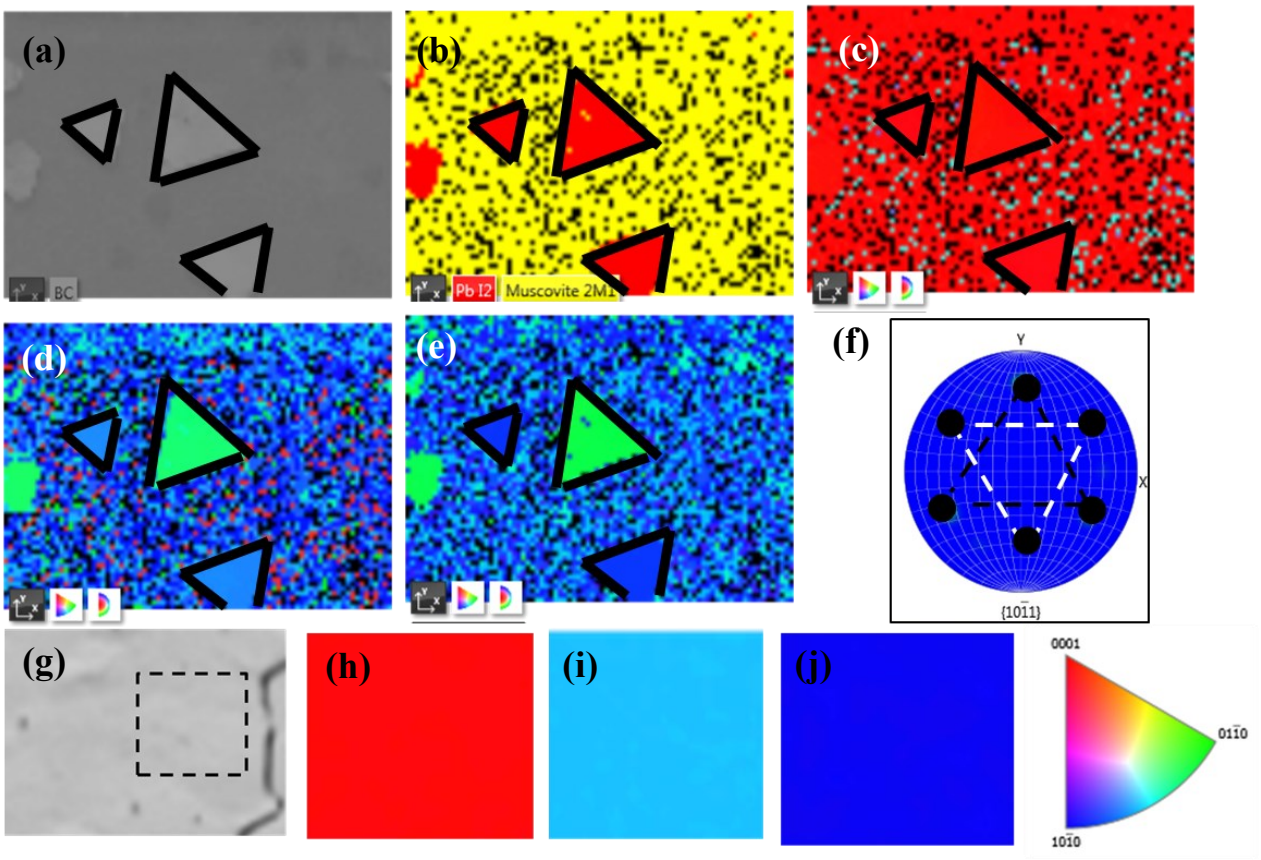

Figure 3. EBSD measurements on uncoalesced PbI_2 triangles and films (a) SEM image of the oriented PbI_2 triangles on mica. (b) Phase mapping showing the PbI_2 region in red and mica in yellow. (c) IPF Z mapping (d) IPF Y mapping. (e) IPF X mapping (f) EBSD pole figure from the sample region. (g) SEM image of the oriented PbI_2 film on mica. (h) IPF Z mapping inside a single domain in a film. (i) IPF Y mapping inside a single domain in a film. (j) IPF X mapping inside a single domain in a film.

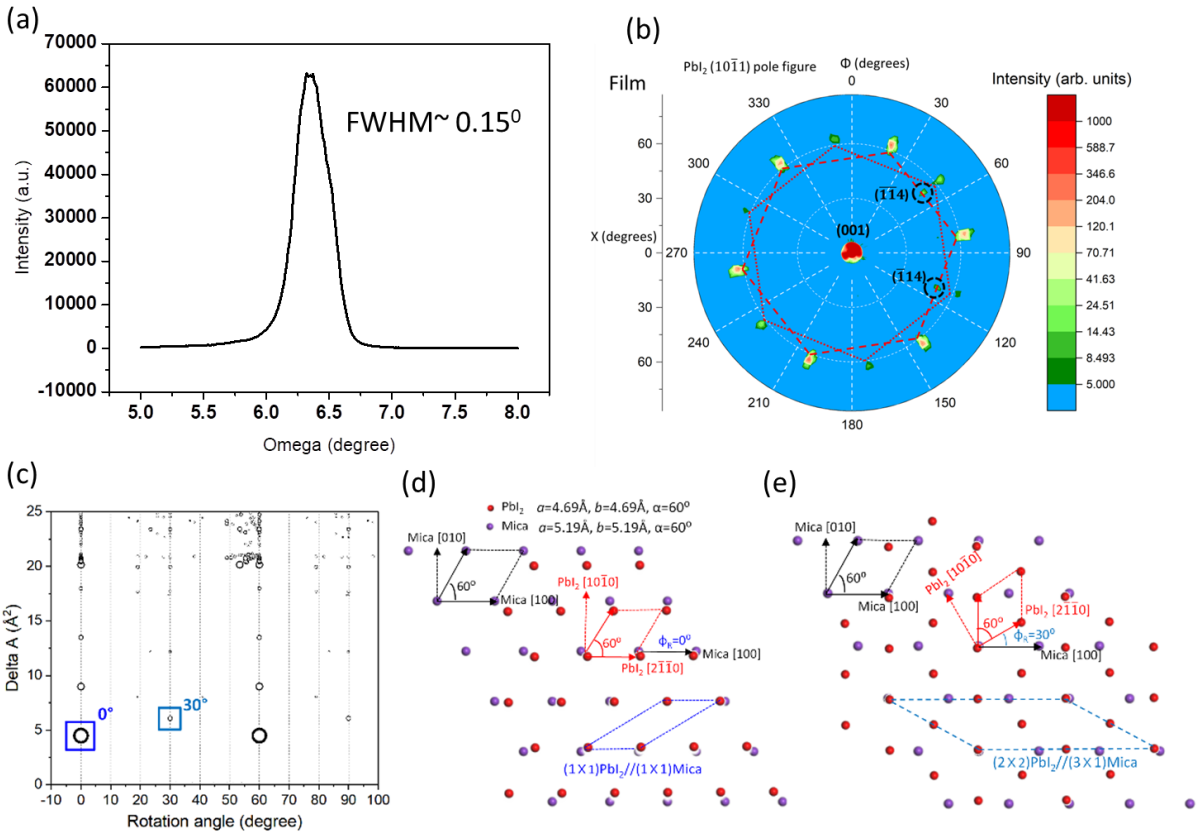

Figure 4. PbI_2 thin film crystal structure characterization for sample grown at ramping rate of 37ºC/min (a) Rocking curve showing dispersion in the out-of-plane direction. (b) Pole figure for the in-plane orientation. (c) Superlattice area mismatch (ΔA) plot for $PbI_2(0001)$ on mica. The rotation angle ϕ_R is defined as the angle between PbI_2 $[2\bar{1}\bar{1}0]$ and mica [100] directions. (d) and (e) 2D lattice overlay for $PbI_2(0001)$ on mica when the ϕ_R are 0º and 30º, respectively, which are the most favorable configurations predicted by the ΔA calculation.

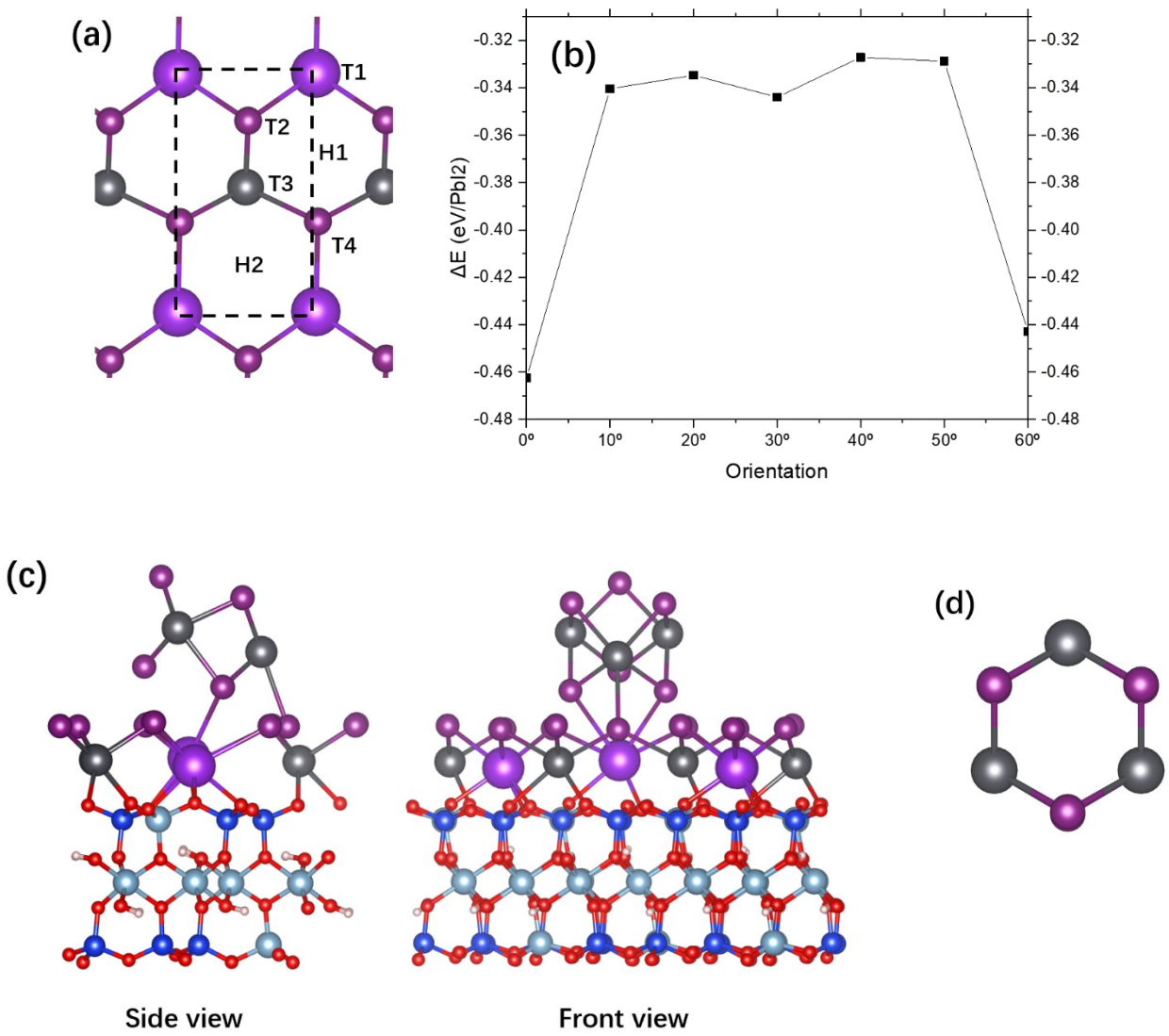

Figure 5. Interaction between PbI_2 ring and the substrate (a) Special positions on the top layers of mica. T refers to the positions on top of the atoms, and H integer refers to the positions on the center of the hexagonal rings. (b) The lowest energy among the various adsorption sites of each PbI_2 formula unit. (c) Configuration of 0º PbI_2 ring located on position T1 after lattice relaxation. (d) Top view of one PbI_2 ring.

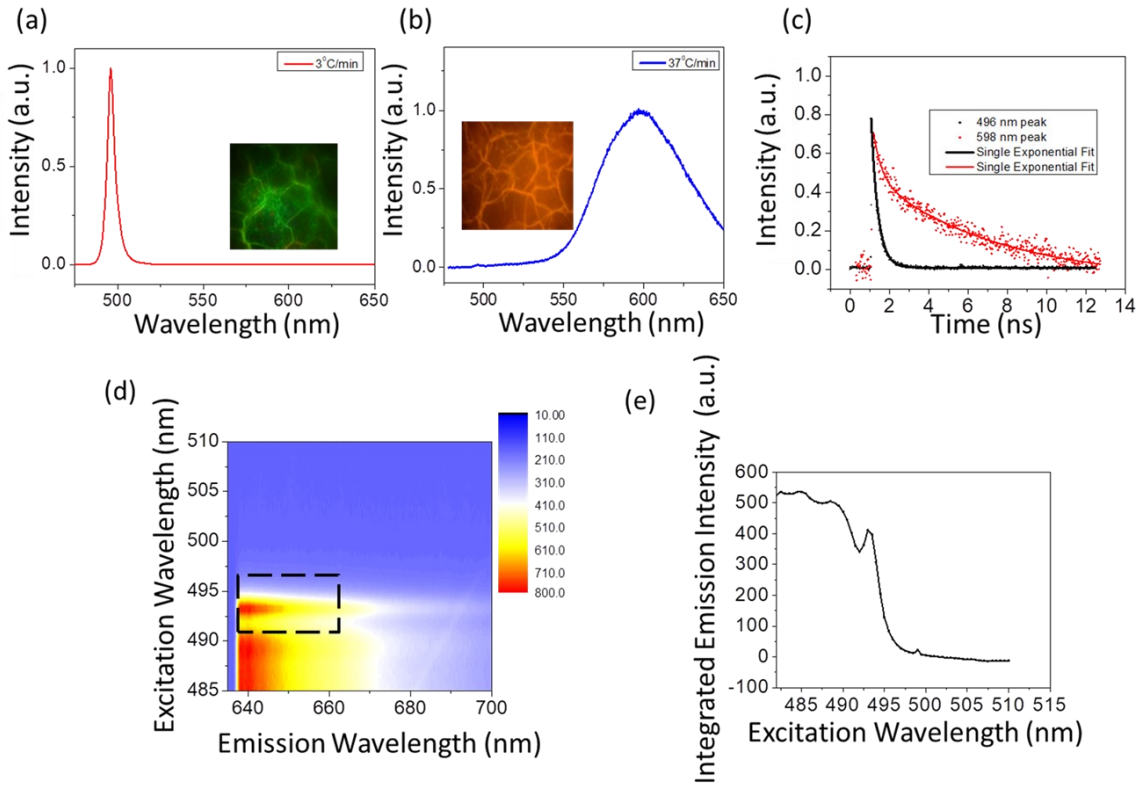

Figure 6. Influence of growth rate on the optical properties of the films (a) PL measurement of film grown at 3 ºC/ min. (b) PL measurement of film grown at 37 ºC/ min. Insets in (a) and (b) show the florescence image of the film (c) TRPL measurement of the PL centered at 598 nm and 494 nm (d) PLE spectra of the sample grown at 37 ºC/ min (e) PLE spectrum for the fixed PL emission centered at 598 nm extracted from (d).

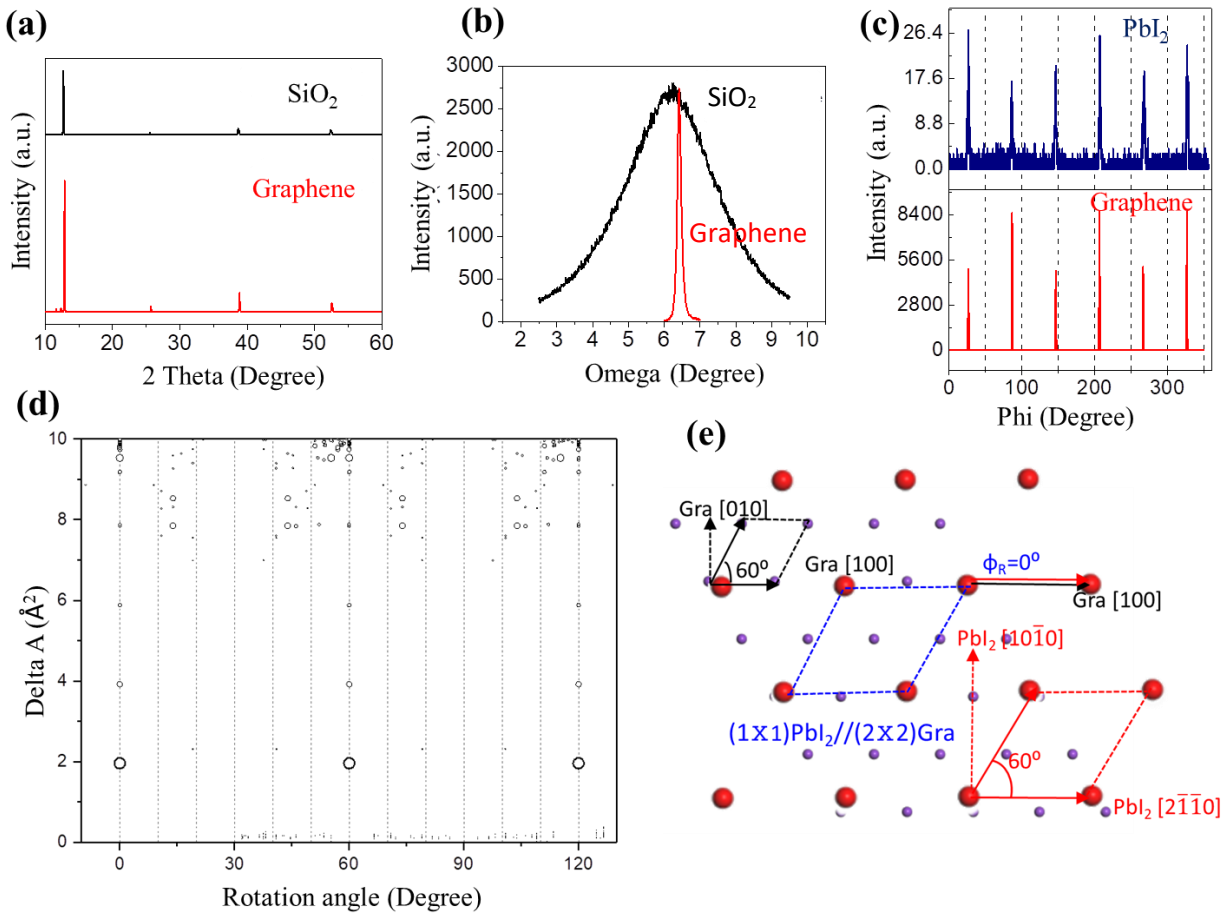

Figure 7. PbI_2 thin film on graphene crystal structure characterization for sample grown at ramping rate of 37°C/min (a) XRD 2θ scan of the PbI_2 film on graphene. The film grown directly on SiO_2 is shown as a reference. (b) Rocking curve showing dispersion in the out-of-plane direction for graphene (red). The rocking curve on SiO_2 is shown in black for comparison. (c) Pole figures for the in-plane orientation. The orientation is compared with the orientation of graphene. (d) Superlattice area mismatch (ΔA) plot for PbI_2(0001) on mica. The rotation angle ϕ_R is defined as the angle between PbI_2 [$2\bar{1}\bar{1}0$] and mica [100] directions. (d) and (e) 2D lattice overlay for PbI_2(0001) on mica when the ϕ_R are 0° and 30°, respectively, which are the most favorable configurations predicted by the ΔA calculation.

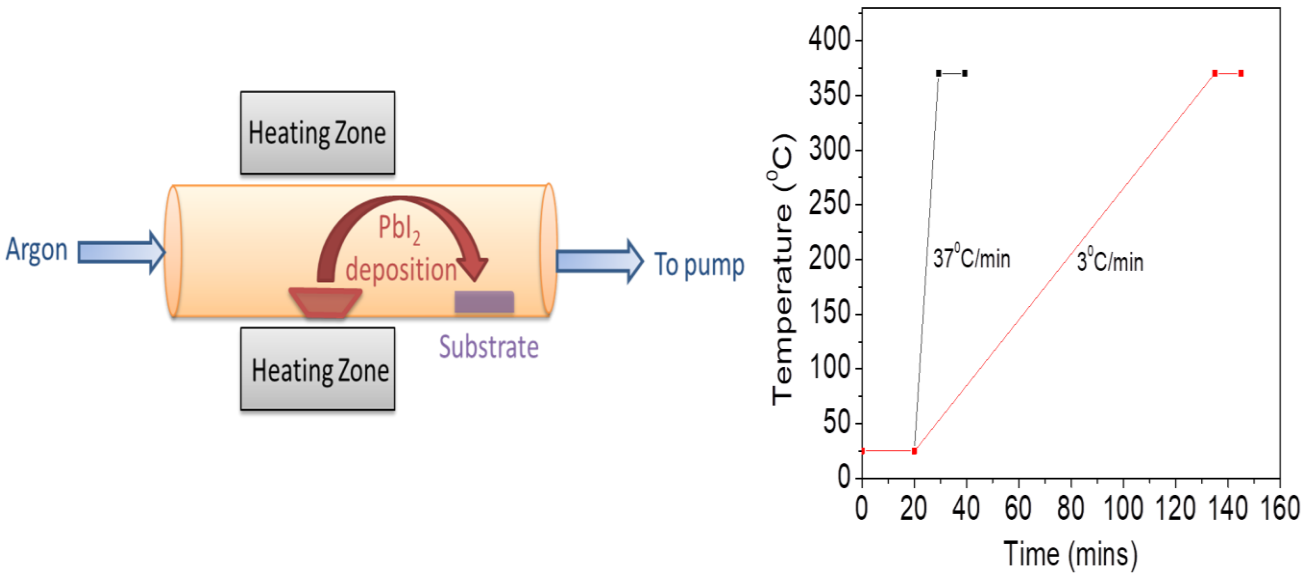

Figure S1. Details of the growth process (a) Schematic of the furnace used for PVD of PbI_2 (b) Temperature profiles for low ramping rate(3^0C/min) and high ramping rate (37^0C/min).

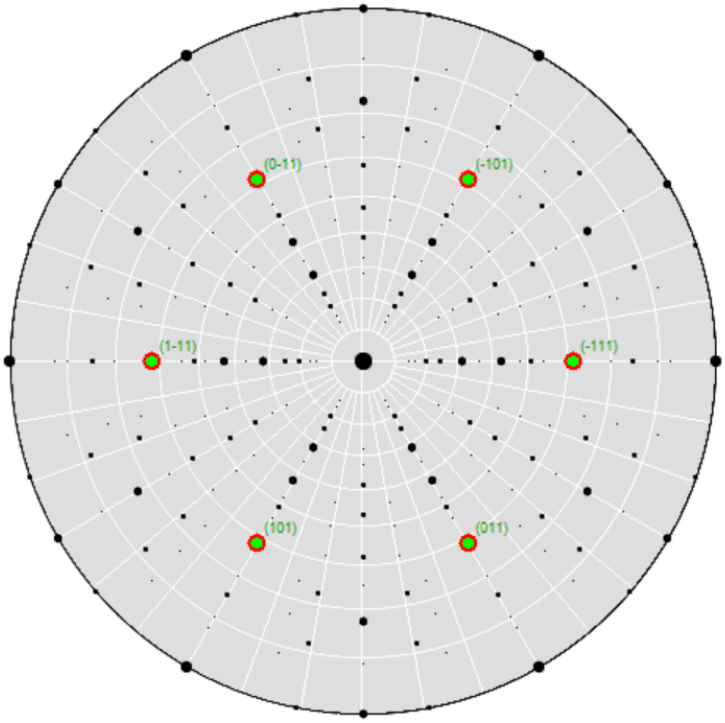

Figure S2. Theoretical pole figure for the {10-11} pole showing the six fold symmetry.

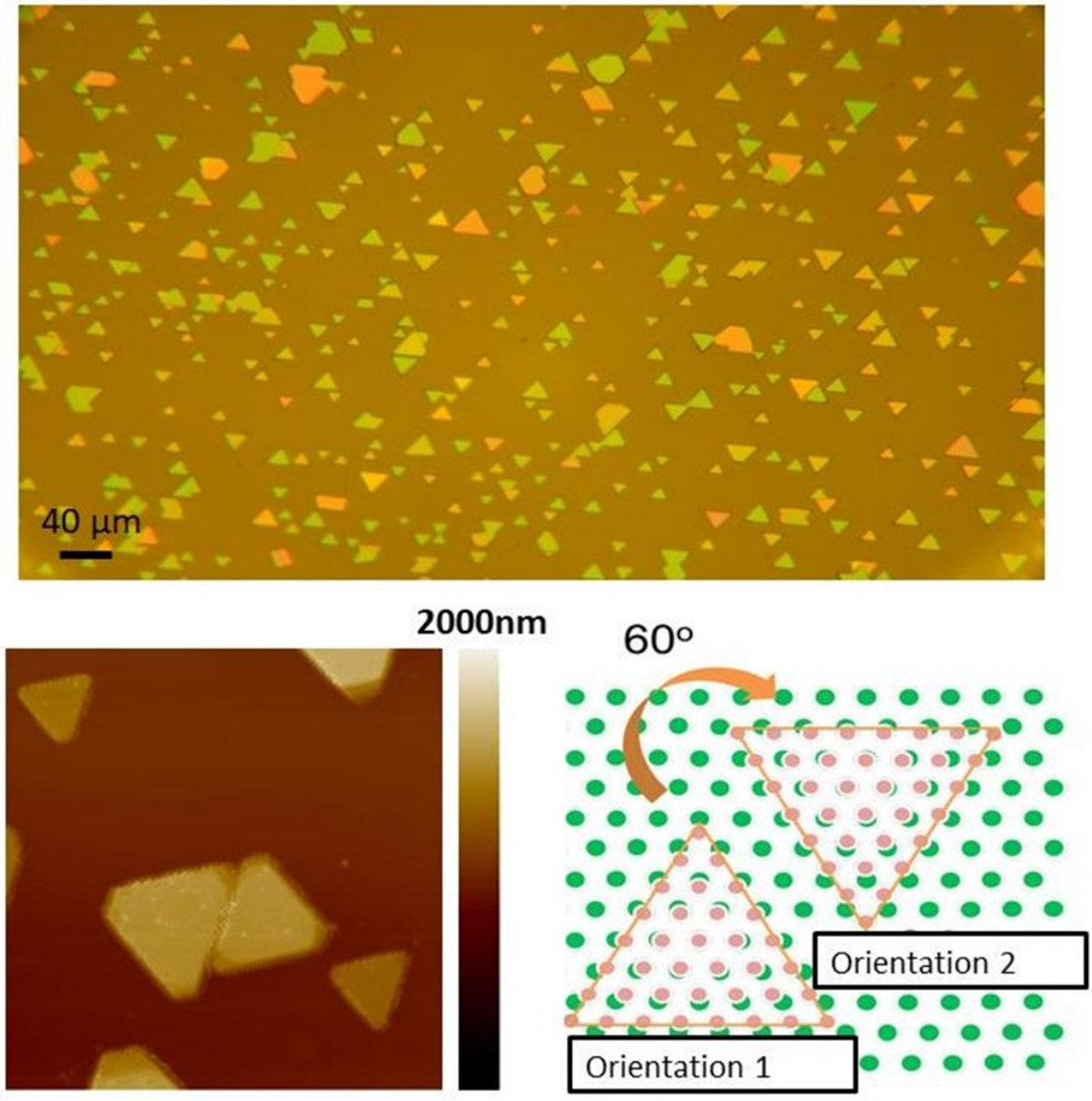

Figure S3. Partial growth resulting in uncoalesced domains (a) Optical image showing triangles with 2 orientations (b) AFM image showing the boundary formed at the interface of the 2 traingles (c) Schematic showing the 2 orientations that are rotated by 60^0 (equivalent to 180^0).

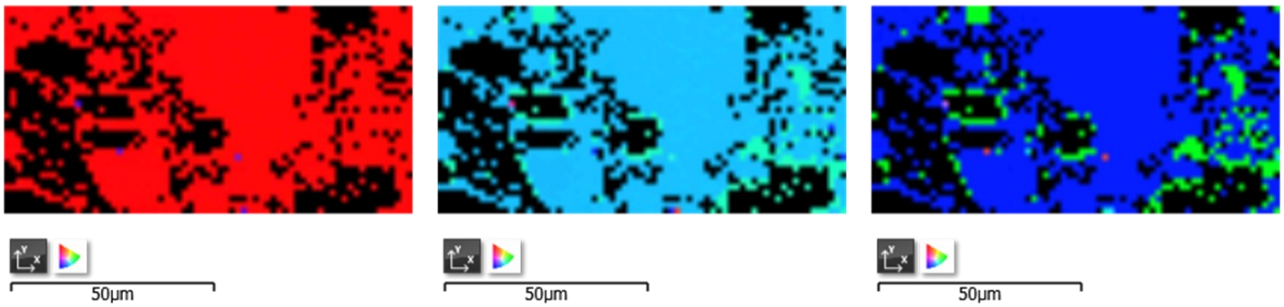

Figure S4. EBSD map inside a single large area domain (a) IPF Z mapping (b) IPF Y mapping (c) IPF X mapping

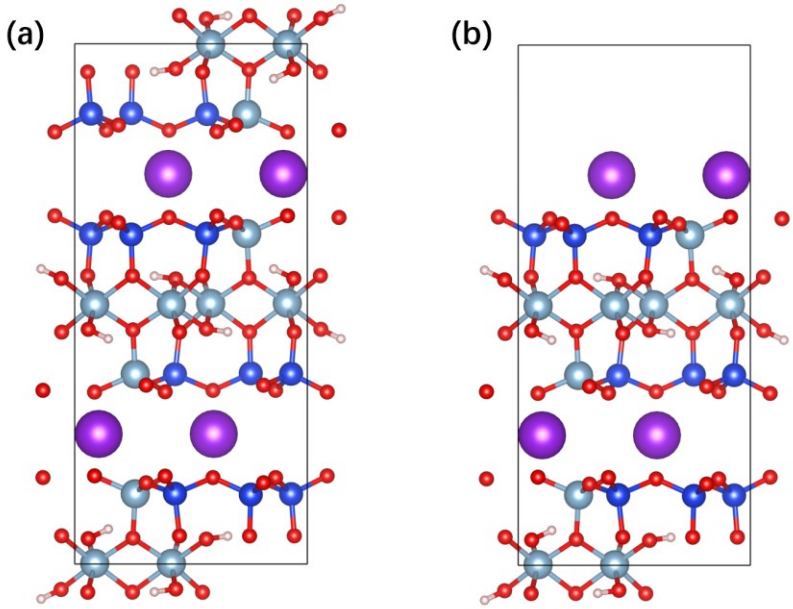

Figure S5. Configuration of mica substrate (a) Configuration of bulk mica. (b) Configuration of mica after cleavage. The big purple atoms are K. The dark blue atoms are Si. The light blue atoms are Al. The red atoms are O. The smallest pink atoms are H.

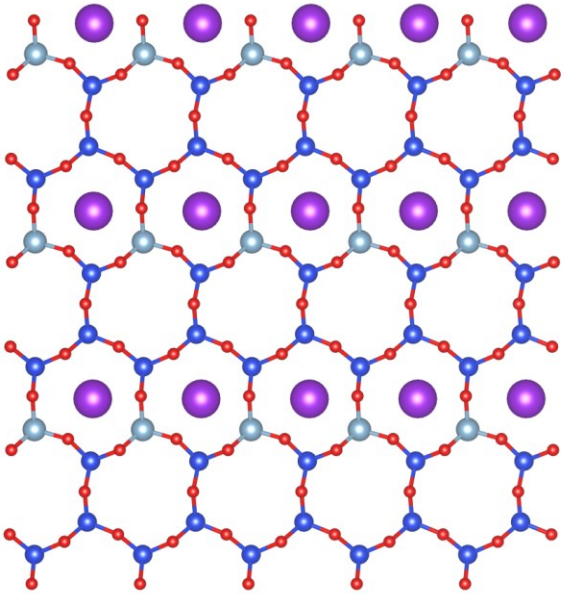

Figure S6. Top view of the surface of mica with half K atoms left on it.

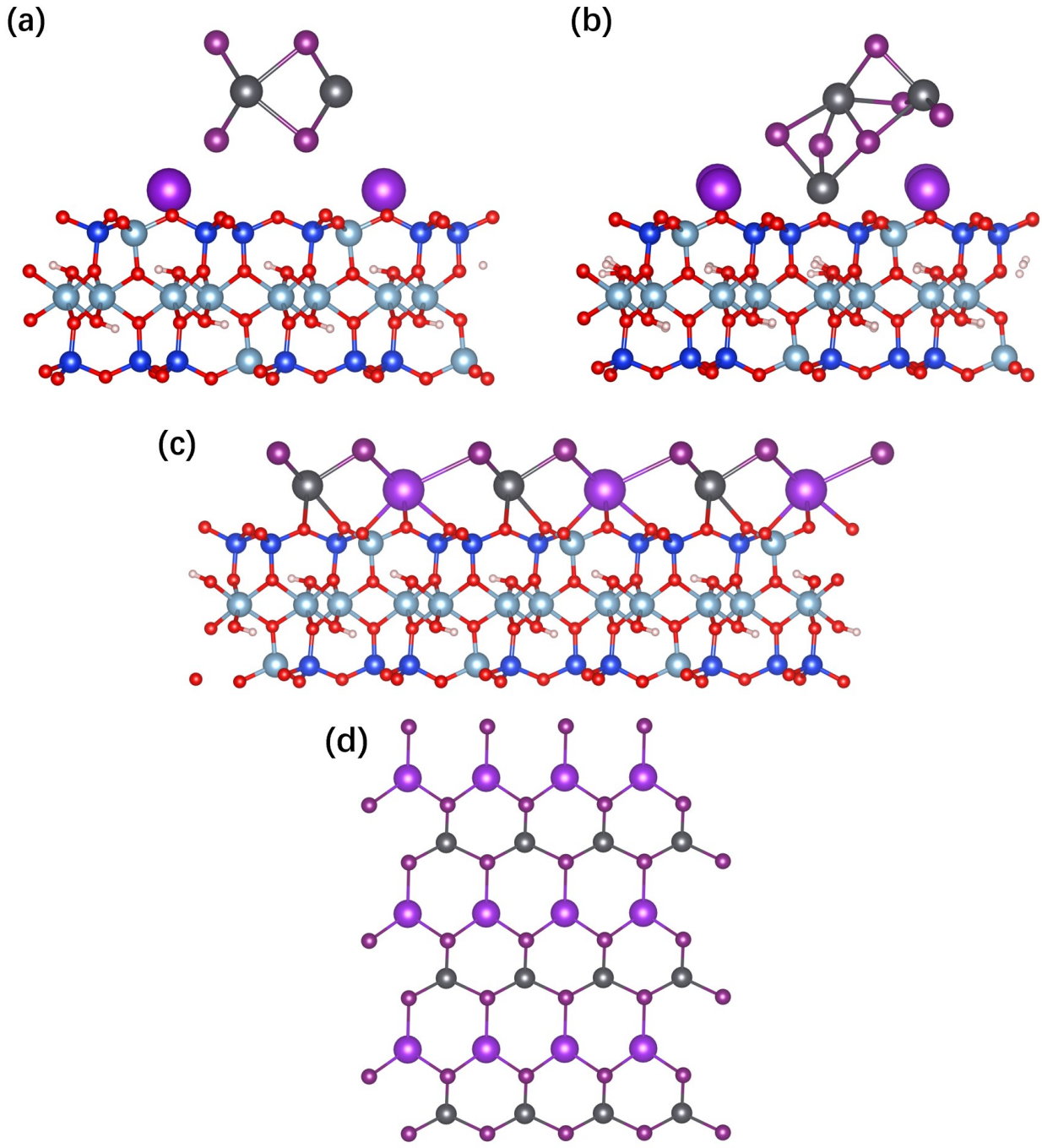

Figure S7. PbI_2 interaction with mica (a) Configuration of PbI_2 ring on two high symmetric positions on mica. (b) Configuration after relaxation. (c) Side view of mica with the vacancies filled with PbI_2. (d) Top view of the surface (only top two layers shown).

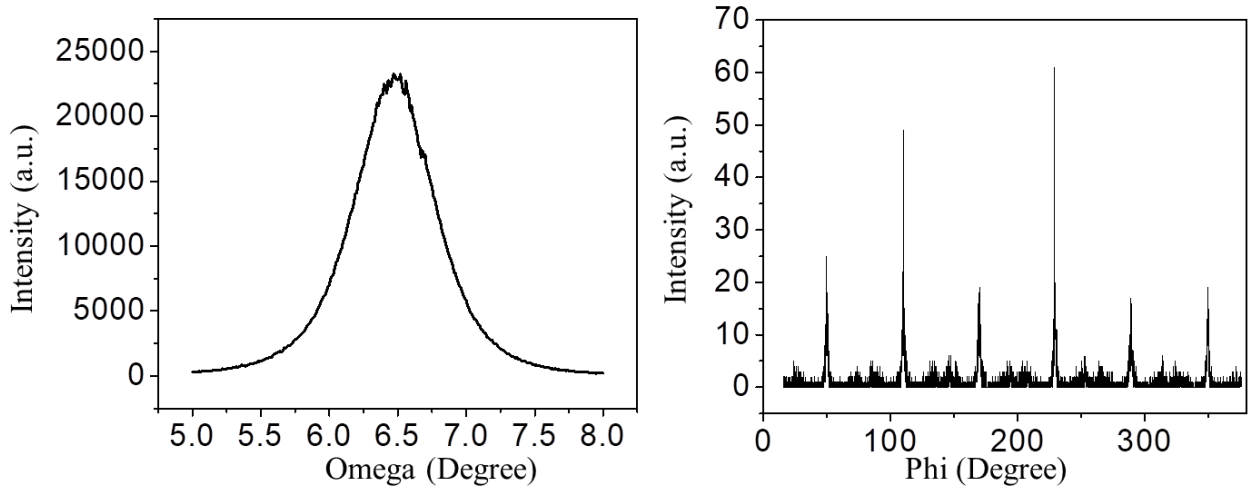

Figure S8. XRD measurements of sample on sapphire (a) Rocking curve showing dispersion in the out of plane direction (b) Phi scans showing dispersion in the inplane direction.

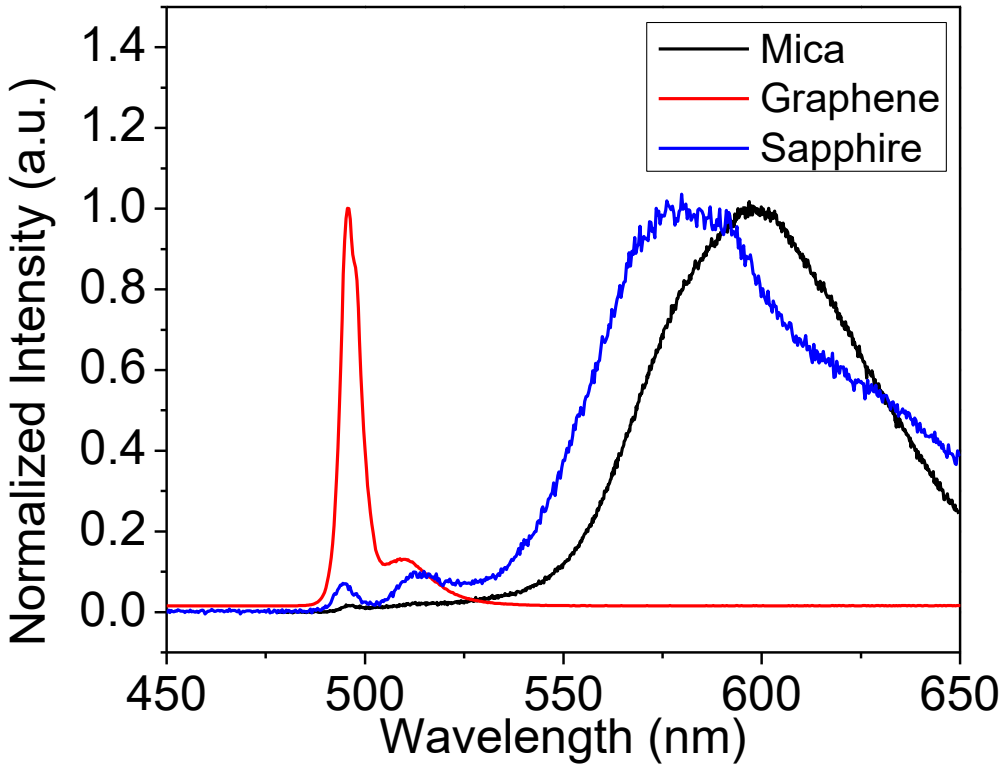

Figure S9. PL measurements on different substrates at a faster ramping rate (37^0C/min). While the sample on graphene shows a sharp excitonic peak, the samples on substrates with stronger interactions (mica and sapphire) show prominent defect peaks.